https://doi.org/10.1016/j.cej.2020.124080

Mitigating the Polysulfides "Shuttling" with TiO_2 Nanowires/Nanosheets Hybrid Modified Separators for Robust Lithium-Sulfur Batteries

Zhen-Dong Huang,‡ Ming-Tong Yang,‡ Ju-Quan Qi, Pei Zhang, Linna Lei, Qing-Chuan Du, Ling Bai, Hui Fu, Xu-Sheng Yang, Rui-Qing Liu, Titus Masese, Haijiao Zhang,* and Yan-Wen Ma**

‡ Z.D. Huang and M.T. Yang contributed equally to this work.

Dr. Z. D. Huang 1, M. T. Yang 2, J. Q. Qi 3, P. Zhang 4, L. N. Lei 5, Q. C. Du 6, L. Bai 7, Dr. R. Q. Liu 10, Prof. Y. W. Ma 13
Key Laboratory for Organic Electronics and Information Displays & Jiangsu Key Laboratory for Biosensors, Institute of Advanced Materials (IAM), Jiangsu National Synergetic Innovation Center for Advanced Materials (SICAM), Nanjing University of Posts and Telecommunications, 9 Wenyuan Road, Nanjing 210023, P.R. China
E-mail: iamywma@njupt.edu.cn
Dr. H. F. Fu 8, Dr. X. S. Yang 9,
Department of Industrial and Systems Engineering, Hong Kong Polytechnic University, Hung Hom, Kowloon, Hong Kong, P.R. China
Hong Kong Polytechnic University Shenzhen Research Institute, Shenzhen, 518057, P.R. China
Dr. T. Masese 11
Research Institute of Electrochemical Energy, National Institute of Advanced Industrial Science and Technology (AIST), Ikeda, Osaka 563-8577, Japan
E-mail: titus.masese@aist.go.jp
Prof. H. J. Zhang 12
Institute of Nanochemistry and Nanobiology, Shanghai University, Shanghai 200444, P. R. China
E-mail: hjzhang128@shu.edu.cn

Abstract: The "shuttling" of the dissolved lithium polysulfides (LPSs) has been a major impediment to the development of a robust lithium-sulfur batteries (LSBs). Functionalization of commercial polypropylene (PP) separators has been considered as a promising alternative strategy for further mitigation of the "shuttle effect" of LPSs. Herein, we re-engineer the surface of PP separator with a sodium-containing TiO_2 hybrid composed of nanowires and nanosheets (STO-W/S), forming a unique sandwich-like surface layer. The polar nature of STO surface layer indubitably improves its wettability to electrolyte, subsequently enhancing Li^+ conductivity. Meanwhile, the synergistic effect of the sandwiched sheet/nanowire hybrid structure, its strong chemical adsorption and the regeneration capability of STO-W/S to LPSs effectively suppresses the "shuttling" of LPSs. As expected, LSBs coupled with STO-W/S

modified PP separators show superior electrochemical performance. They deliver high discharge capacity of 813 mAh· g^{-1} at 1C and superior cycling stability with a capacity fading rate of 0.067% for each cycle, and the capacity was still maintained at ~ 541 mAh· g^{-1} for 500 cycles. Based on the aforementioned advantages, this newly-proposed functionalization strategy for separators can be a promising route to develop the next-generation multifunctional separators for high-performance LSBs.

Keywords: TiO_2; Surface engineering; Separator; Shuttle Effect; Lithium-sulfur batteries

1. Introduction

As the world is gearing towards clean energy, the demand for largescale, high-density energy storage systems is on the continuous rise.[1-3] Lithium-Sulfur batteries (LSBs) are considered to be a viable option to satisfy the high demand of power storage systems, due to their significantly higher energy density compared to conventional lithium-ion batteries.[4-6] However, the feasibility of LSBs is greatly undercut by their low efficiency and short cycle life.[7-9] This is largely attributed to the "shuttle effect" of soluble lithium polysulfides (LPSs) from cathode to the surface of lithium anode, which is a parasitic reaction that leads to the capacity fading of LSBs.[10] To address this issue, energy scientists have attempted to design the sulfur reservoirs from metal nitrides, metal oxides, porous carbon materials and their composites or heterostructures into a variety of three-dimensional structures akin to 'fishing nets' in order to prevent LPSs (analogous to the 'fish') from escaping from the sulfur cathode.[11-15] Even so, there are some LPS 'fish' that still manage to escape from the 'fishing net'. Therefore, the separators for LSBs are meant to function as the second 'customs pass' to selectively prevent the passage of LPSs from the cathode to the anode side,[16-18] as demonstrated in **Figure 1a**. Otherwise, the escaped LPSs will be continuously depleted (or 'killed') on the surface of lithium metal anode and thus become 'dead fishes'. This excessive loss of active sulfur from cathode is one of the key factors that accounts for the relatively poor cycling stability of those reported LSBs.[19-21]

Besides being the key safety components, separators also have other crucial functionalities in various types of batteries. [22] In addition to their isolation role, battery performance metrics, namely rate capability, cycling performance and safety at elevated temperature, can be also influenced from some key properties of the separator such as their wettability to the liquid electrolyte, thermal stability, and interface compatibilities with both the cathode and anode.[22-25] Notwithstanding, the separator's categorical role in LSBs is to act as the second 'customs pass' to selectively prevent the passage of LPSs from cathode to anode side.

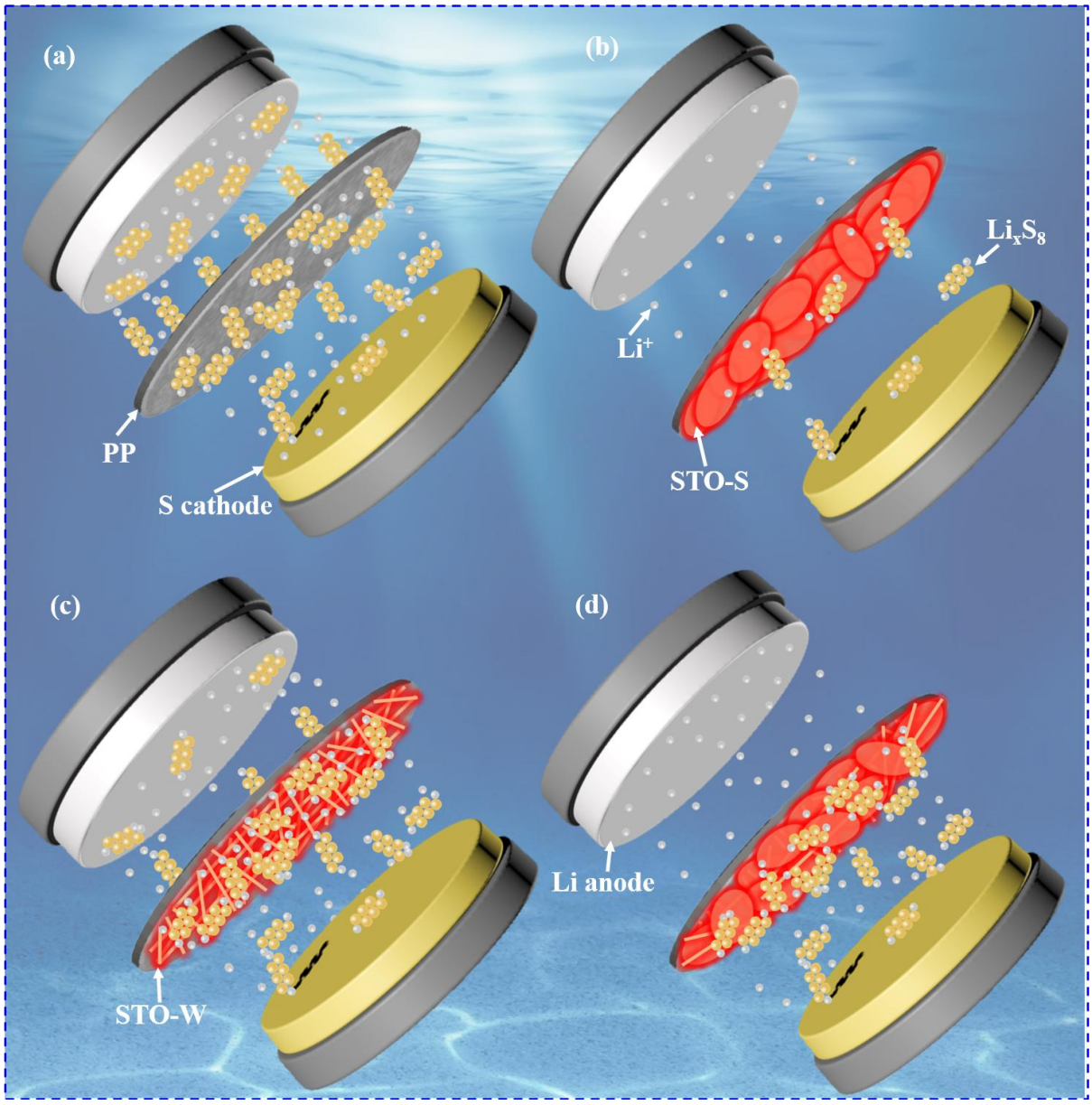

Figure 1. The schematic illustration of the configuration of LSBs and the suppressive effect to the shuttle of LPSs with the PP separator (a), and PP modified with STO-S (b), STO-W (c), and STO-W/S hybrid (d), respectively.

Currently, to circumvent the "shuttle effect", it is common to apply a blocking layer and/or an adsorption regeneration layer in order to functionalize the commercial polyolefin separators (including polypropylene (PP) and polyethylene and their multilayer hybrid membranes).[26-30] For example, due to the strong charge repulsion to the LPS of the negatively charged GO and Nafion surface, Nafion-modified ultra-thin graphene oxide (GO) layers have been applied as coating to block the large channel within the polyolefin separators to suppress the 'shuttling'

of LPSs through the transmembrane.[10] In addition, Metal-organic frameworks,[2] Phosphorus,[3, 21] 0D (nanoparticles)/1D (nanofibers) composite layers,[4, 8] MoS_2,[5] layered double hydroxide,[7] Titania and Titanate, [18,19,25,26] Mxene,[27] conductive polymer,[28] and their carbon composites,[10,17,29] formed from zero-, one-, two- and three-dimensional nanomaterials containing N, P, O and Ti, have been used judiciously in the design of adsorption regeneration layers on the cathode side of the separator to constrain, the "shuttle effect" of LPS to some extent.

Moreover, the good film-forming and adhesion properties of two-dimensional sheet-type materials and the one-dimensional nanowires/fibrous materials are helpful to engineer the hydrophobic smooth surface of polyolefin separators. [16, 22, 27, 29, 31, 32] However, the modification coating built by the pure sheet-like materials, for instance, the GO layered films, which are extremely dense structures with smooth surfaces, block both the transportation of Li^+ and LPS, [32] as demonstrated in **Figure 1b**. In contrast, the porous coating formed by the randomly distributed nanowires/fibrous materials allows the quick passage of Li^+ and LPS simultaneously, [16, 22, 31] as shown in **Figure 1c**. Thus, the two-dimensional porous carbon, the graphene-based mixture and sandwiched structure, carbon nanotubes/fibers-based composite have been applied to modify the surface of commercial polyolefin separators with the aim to overcome the aforementioned intrinsic structural problems. [4-10, 18, 32]

Herein, a novel functional layer made of sodium-containing titanium oxides nanowires/nanosheets (hereafter known as STO-W/S) hybrid has been designed and engineered on the surface of polypropylene (PP) separator toward cathode to suppress the "shuttling" of dissolved polysulfides to the lithium anode. Taking advantages of the sandwiched unique structure of STO hybrid of nanowires and nanosheets, as well as the chemical nature of the strong chemical adsorption capability of the polar STO to LPSs, it is expected that Li^+ transportation will be facilitated, but the passage for LPSs will be blocked,

as clearly demonstrated in **Figure 1d**. The STO-W/S hybrid containing both STO-W and STO-S was prepared via one-pot route by controlling the synthetic conditions of hydrothermal process, rather than by physical mixing of STO-W and STO-S. Interestingly, the electrochemical measurement results further corroborated our initial hypothesis. By making use of the permselective function of the newly-developed STO-W/S hybrid modified PP separators, the expected improvements on the cyclic stability, the capacity and rate capability of LSBs have been achieved.

2. Experimental Section

One-pot preparation of STO-W and STO-W/S： A modified hydrothermal method was applied to develop the desired STO-W and STO-W/S. In a typical preparation procedure, 0.3 mol of sodium hydroxide (AR, Sinopharm Chemical reagent) was initially dissolved into 30 ml distilled water to obtain a 10 $mol \cdot L^{-1}$ of strong alkaline solution under magnetic stirring on a hot plate (MYP11-2) for 30 mins. Subsequently, 6 millimol of tetrabutyl titanate (AR, Lingfenghx) was dropwise added into 30 ml absolute ethanol (AR, Yasheng-Chem) under continuously magnetic stirring to form a 2 $mol \cdot L^{-1}$ solution. After that, the obtained alkaline solution was poured into the as-prepared tetrabutyl titanate solution under intense magnetic agitation, followed by 30 mins ultrasonication treatment to obtain a uniformly dispersed mixture. Then, the dispersed mixture was sealed into 100 ml Teflon-lined stainless steel hydrothermal autoclave reactors. Subsequently, the sealed reactors were put into the blast drying oven (DHG-9035A) pre-heated to 190 ^{o}C for 8 to 18 h to optimize the synthetic condition of the desired STO-W and STO-W/S. Upon cooling to room temperature within the furnace, the precipitated white products were collected, and subsequently purified and washed three times with diluted hydrochloric acid and distilled water, respectively. Hydrogenated sodium titanate was obtained upon drying at 60 °C oven for 24 h. The final STO-W and STO-W/S were obtained by thermal treatment of the corresponding hydrogenated sodium titanate precursors at 550 °C for 10 h under argon atmosphere in a tube furnace.

Modification of PP separators: In a typical surface engineering process, 150 mg of the as-prepared STO-W and STO-W/S powders were initially re-dispersed into 450 ml absolute ethanol to get a uniform and stable dispersion of 0.33 $g \cdot L^{-1}$ with the addition of 450 mg polyvinylpyrrolidone (PVP) as dispersant by ultrasonication for 1 h. Subsequently, ~3 ml of the obtained dispersion were poured into a 20 mm sand core funnel with PP separator (Celgard 2325) as filter paper followed by a flow-directed vacuum filtration self-assembling process. The thickness of the surface layer on PP separator was determined by fixing the size of funnel and the taken volume of STO-W and STO-W/S dispersion. After filtration, the resultant membranes were dried at 40 ^{o}C for 24 h with filter papers in a blast drying oven. Finally, the modified membranes were collected and punched into 19 mm discs as the separators for LSBs.

Characterization of physicochemical properties: Morphology and microstructure of the as-prepared STO-W and STO-W/S and the modified separators was analyzed using a field-emission scanning electron microscope (FE-SEM, Hitachi S-4800) at an acceleration voltage of 3 kV and high-resolution transmission electron microscopy (HRTEM, FEI Talos F200X S/TEM) at an acceleration voltage of 100 kV. The compositions and elemental mapping of the as-prepared STO-W and STO-W/S were detected by the energy dispersive spectroscopy (EDS) detectors coupled to the FEI Talos S/TEM. X-ray diffraction (XRD) patterns of the as-prepared Titanium compounds (STO-W and STO-W/S) were measured on an X-ray diffractometer (Bruker D8 Advance A25) using Cu–Kα radiation (λ = 1.54060 Å). The diffraction patterns were recorded in a 2θ range of 10–80 ^{o} with a step size of 0.02 ^{o}. The optical photos of the different separators at different conditions were taken using a digital camera.

Measurements of electrochemical performance: The AC-S composites were first prepared through a melt-diffusion method, whereby 66.7 *wt.*% S and 33.3 *wt.*% of AC were ground,

sealed into a Teflon-lined stainless steel autoclave filled with Ar gas and annealed in the blast drying oven at 155 °C for 12 h at a heating rate of 1 ^{o}C min^{-1}.

The AC-S composite cathode was prepared using a mixture of 80% AC-S, 10% acetylene black, and 10% poly (vinylidene difluoride) (PVDF) in N, N-methylprrrolidone as solvent. Celgard 2325 membranes and 1 mol· L^{-1} LiTFSI dissolved in 1, 2-dimethoxyethane/1, 3-dioxolane (DOL : DME = 1 : 1 by volume) with 1 % $LiNO_3$ additive were purchased from DoDoChem and used as separator and electrolyte, respectively. The applied ratio between electrolyte and mass loading of S within the cathode was ~ 20 μL· mg^{-1}. The CR2032 coin cells were assembled in an Ar-filled glove box (LABstar, MBRAUN) with lithium foils as the counter electrodes. Cycling performance tests were conducted in a Land CT2001A battery system at a voltage range of 1.7–2.8 V. Note that the capacity was based only on the mass of sulfur alone. Cyclic voltammograms were measured using a VMP3-Bio-Logic multi-channel potentiostat at a scanning rate of 0.05 mV · s^{-1} in a voltage range of 1.7–2.8 V. Electrochemical impedance spectroscopy (EIS) was carried out in a frequency range of 0.01 Hz to 100 kHz, and the perturbation amplitude was set at 5 mV.

3. Results and discussion

3.1. STO-W and STO-W/S

To verify the feasibility and superiority of using the hybrids of nanowires and nanosheets to modify the commercial PP separator for LSBs, the sodium-containing titanium oxide nanowires and their hybrids with nanosheets, namely STO-W and STO-W/S, were successfully prepared by an optimized one-step hydrothermal method. As shown in **Figures 2a-2c,** with the extension of the hydrothermal reaction duration from 8 h to 11 h at 190 ^{o}C, the obtained nanowires become more uniform and longer. Moreover, the STO-W synthesized via a reaction duration of 11 h also assume a bamboo-raft-like nanowire array (see **Figure 2c**).

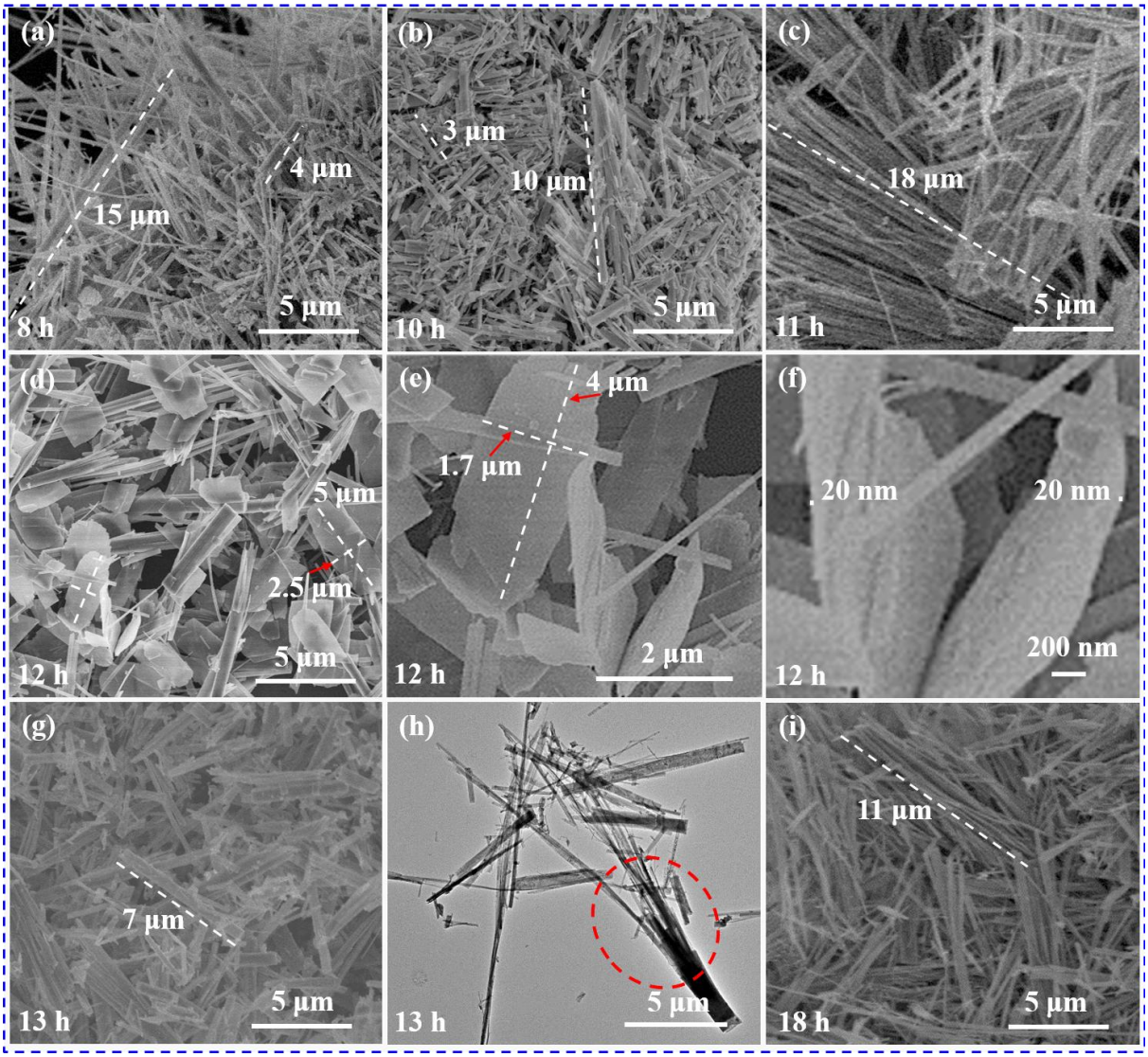

Figure 2. SEM images of as-prepared STO prepared at 190 ^{o}C for 8 h (a), 10 h (b), 11 h (c), 12 h (d, e, f), 13 h (g, h) and 18 h (i), respectively.

When the reaction time was further extended to 12 h at 190 ^{o}C, the desired hybrids of nanowire and nanosheets were formed. The thickness of the obtained nanosheets was about 20 nm. The length and width of the nanosheets were ~2 and 5 µm, as illustrated in **Figures 2d-2f**. With the extension of hydrothermal reaction time to 13 h, STO nanosheets further disintegrated into nanobelts and nanowires, as shown in **Figures 2g** and **2h**. The STO sample prepared at 190 ^{o}C for 18 h fully became nanowires, as illustrated in **Figure 2i**. However, the extensive array structure found from the STO-W-11h was not observed in the SEM image of as-prepared STO-W-18h (**Figures 2c** and **2i**). Therefore, STO-W-18h was chosen as

controlled materials to modify the PP separators. Unless directed otherwise, the STO-W hereafter denotes STO-W-18h. The results observed above indicate that the STO-W and STO-W/S can be obtained by optimizing the hydrothermal reaction duration.

In order to further assess the composition and crystal structure, as-prepared STO nanowires and nanosheets were analyzed by high-resolution scanning/transmission electron microscopy (HR-S/TEM) coupled with high-resolution element mapping and X-ray diffraction (XRD). HR-S/TEM and element mapping images, presented in **Figures S1a-S1h**, indicate that a small amount of sodium still remained in the final titanium oxide products after being washed with hydrochloric acid. The atomic sodium content within the STO-W and STO-S are about 10 % and 1%, respectively. This observation is also confirmed by the analysis results of crystal structures. As shown in **Figure 3a**, the obtained XRD patterns of both STO-W and STO-W/S indicate that both STO-W and STO-W/S contained two main phases of titanium oxide, namely monoclinic brookite-type TiO_2 (TiO_2 (B)) and tetragonal anatase TiO_2. Normally, the TiO_2 (B) could be prepared through dehydration of titanate radical, which is derived from the de-sodiation of sodium titanate, such as monoclinic $Na_2Ti_9O_{19}$ in this work. Based on the higher sodium content and the XRD peaks indexed to monoclinic structure, the proportion of monoclinic TiO_2 (B) within STO-W was higher than that within STO-W/S.

Figure 3b shows the HRTEM image of STO nanosheets. **Figure 3c** is the fast Fourier transformation (FFT) images taken from the red dash square in **Figure 3b**. This observation further clarifies that STO nanosheets consists of three phases. The monoclinic TiO_2 (B) is along the [001] zone axes labeled as white line while the tetragonal TiO_2 is along [010] zone axes labeled as green line. The $Na_2Ti_9O_{19}$ phase is marked as solid red circle in the FFT image. The FFT results are consistent with the single crystal electronic diffraction patterns of monoclinic TiO_2 and tetragonal TiO_2 as shown in **Figures 3d** and **3e**, respectively. The HRTEM image of STO nanowire is shown in **Figure 3f**. The FFT image given in **Figure 3g** taken from the red dash square in **Figure 3f** indicates that the STO nanowires are also

composed of monoclinic TiO_2, tetragonal TiO_2 and $Na_2Ti_9O_{19}$ phase. **Figures 3h** and **3i** are the inverse fast Fourier transformation (IFFT) images of monoclinic TiO_2 and tetragonal TiO_2, respectively. The atomic level microstructure of monoclinic TiO_2 is taken along the [001] zone axes while the atomic-resolution tetragonal TiO_2 is along [010] zone axes.

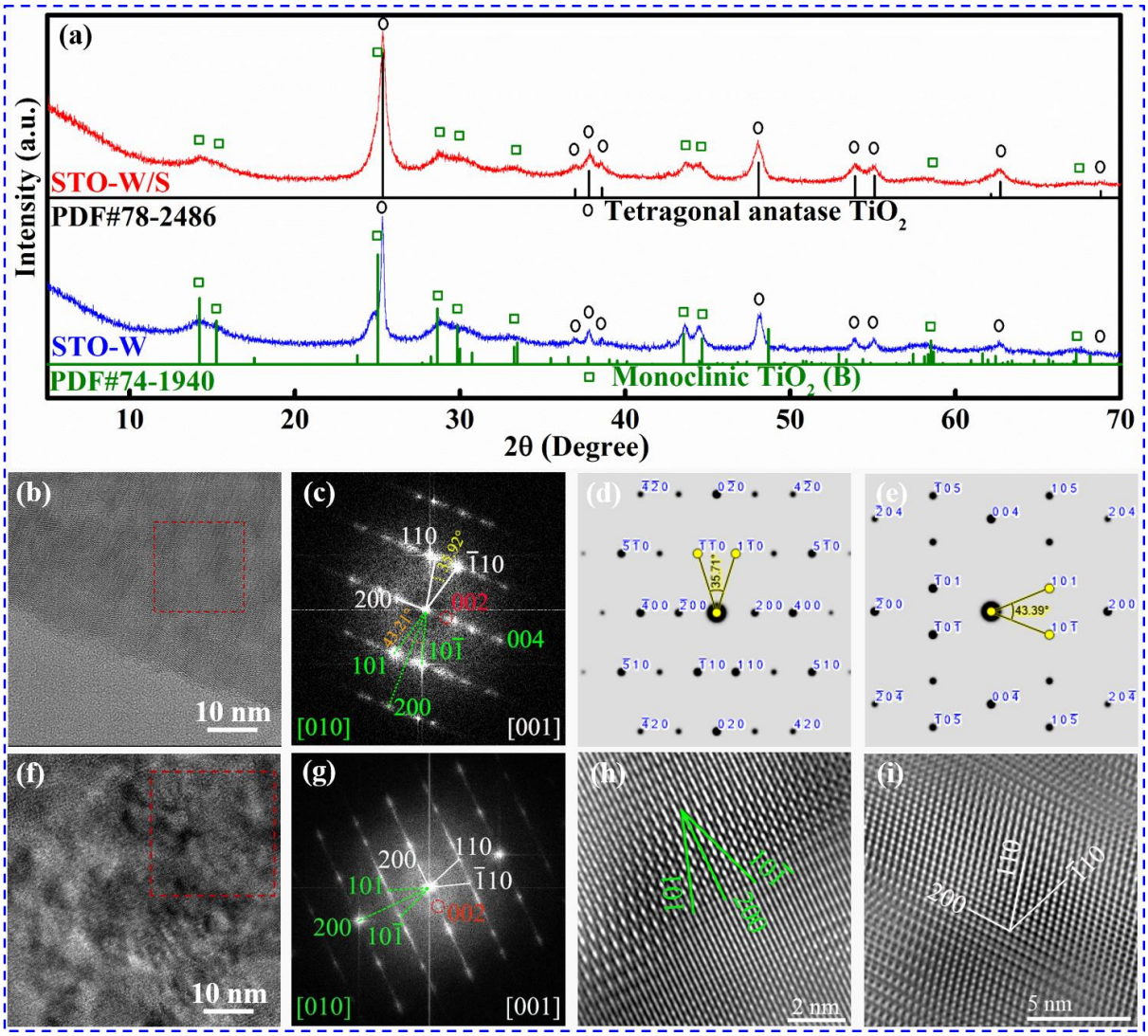

Figure 3. XRD patterns (a), HRTEM images (b, f) and FFT images (c, g) of STO-S and STO-W, respectively; the single crystal diffraction patterns (d, e) and (IFFT) images (h, i) of the observed monoclinic TiO_2 and tetragonal TiO_2, respectively.

2.2. PP separators engineered with STO-W and STO-W/S surface layer

Figure 4 presents the optical images of PP separator, STO-W and STO-W/S modified PP separators at the original, wetting, wetted, twisted, and unfolded state, respectively.

Comparing to original PP separator, the separators become dark and light brown after being modified with STO-W and STO-W/S, respectively, as shown in **Figures 4ai, 4bi** and **4ci**. Furthermore, since the wetting properties of separators significantly influence LSBs' electrochemical performance, the electrolyte wettability of PP, STO-W and STO-W/S modified PP separators were further investigated. As shown in **Figure 4aii** and **4aiii**, the electrolyte could not fully wet the PP separator, due to the low porosity and the non-polar characteristics. An electrolyte droplet could still be seen on the surface of PP separator after 2 min. It is however interesting to note that both of the modified PP separator exhibit excellent wettability with the applied electrolyte. The dropped electrolyte was quickly and completely absorbed by the modification layer of STO-W and STO-W/S and uniformly spread over the modified separators poles, as shown in **Figures 4bii, 4biii, 4cii** and **4ciii**. Apart from the excellent electrolyte wettability, both of the modified separators maintain essentially the same mechanical property with original PP separator. No obvious cracking and peeling were found from the separators expanded from seriously twisted PP separators, as observed from **Figures. 4aiv, 4av, 4biv, 4bv, 4civ** and **4cv**.

Figures 4di, **4dii**, **4ei** and **4eii** present the top view TEM images and the cross-section view SEM images of STO-W and STO-W/S modified PP separators, respectively. In transmission mode, many through-holes can be observed from the top view TEM images shown in **Figure 4di**, which would be not good for suppressing the shuttle effect of LPSs. As expected, no through holes can be found from the top view TEM images shown in **Figure 4ei**. This result manifests that the hybrid structure of nanowires and nanosheets is relatively desirable for constructing a permselective nanostructure for Li^+, instead of LPSs, on the cathode side of the PP separator, which will vastly improve the cyclic stability, the capacity and rate capability of LSBs, as illustrated in **Figure 1**. Meanwhile, the hybrid structure of nanowires and nanosheets of STO-W/S is also helpful for obtaining a thinner and dense modification layer on top of the PP separator, since a higher pressure can be created during the preparation of modification

layer by using vacuum filtration process. As illustrated in **Figures 4dii** and **4eii**, the thicknesses of the STO-W and STO-W/S functional layer are about 6.7 and 4.4 μm, respectively. The thinner the modification layer, the smaller the effect on energy density. Therefore, the PP separator modified by the hybrid of STO-W/S functional layer would be a desired separator for LSBs, based on the structure and strong chemical absorption capability of STO-W/S functional layer.

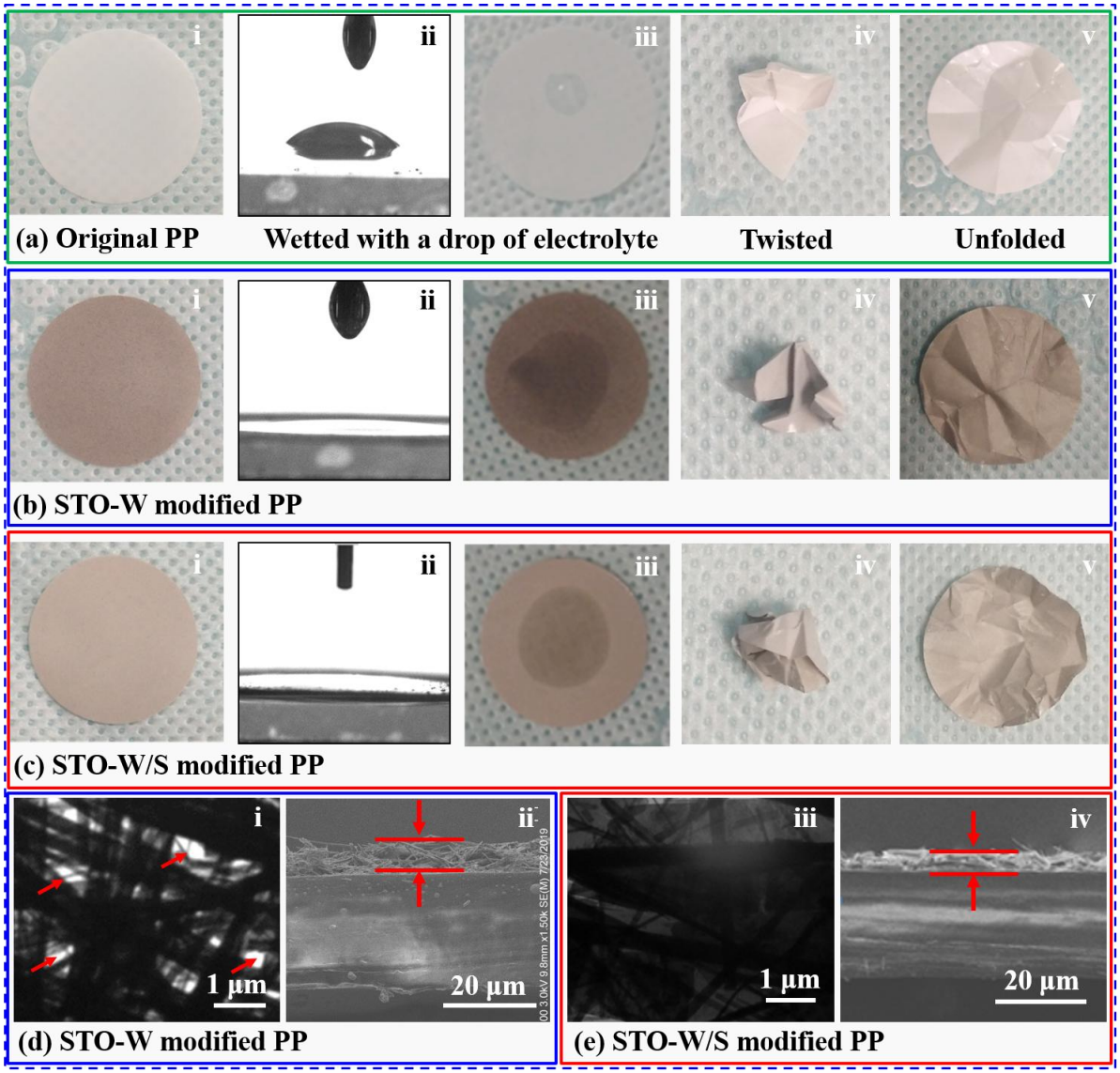

Figure 4. Optical images of original (i), wetting (ii), wetted (iii), twisted (iV), and unfolded (V) PP separator (a), STO-W modified PP separator (b), and STO-W/S modified PP separator (c), respectively; the top view TEM image (i) and the cross-section view SEM images (ii) of STO-W (d) and STO-W/S (e) modified PP separators, respectively.

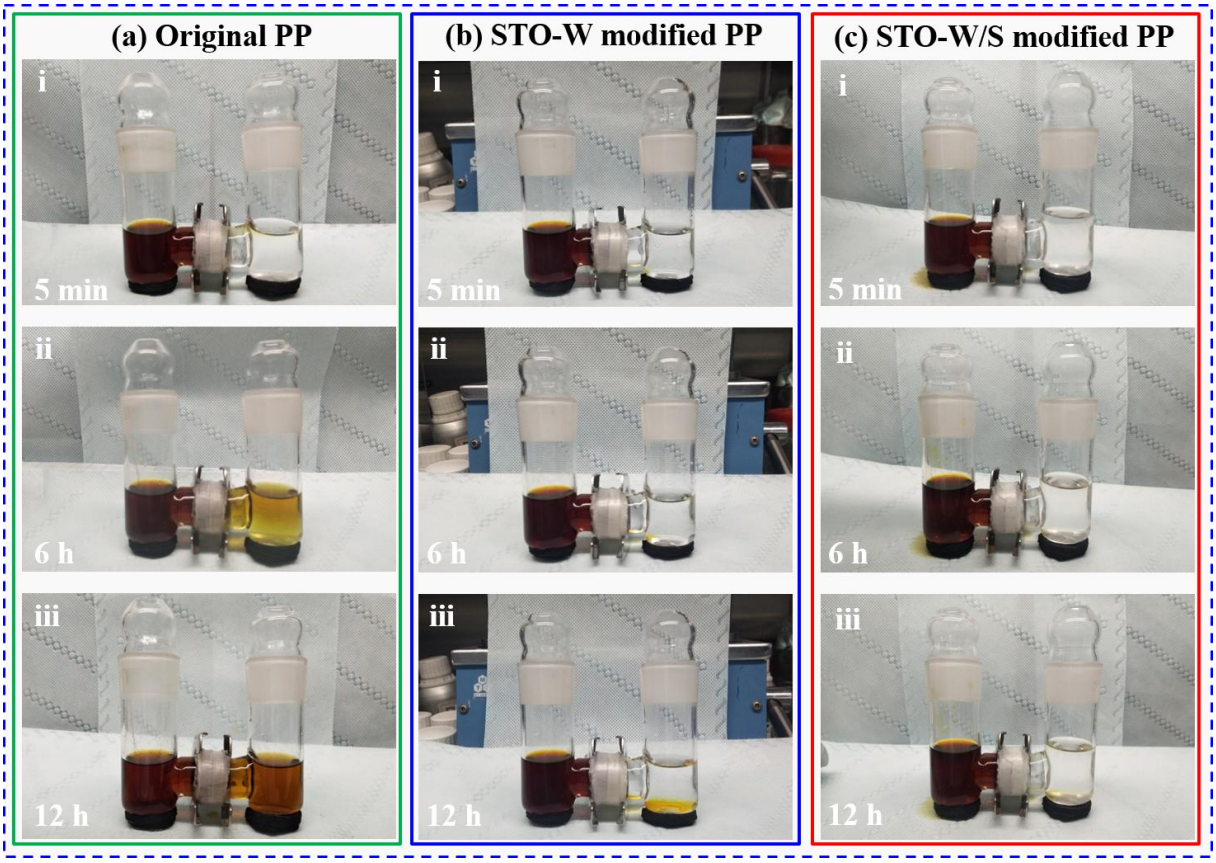

Figure 5. Lithium polysulfide permeation measurements for the original PP (ai – aiii), STO-W (bi – biii) and STO-W/S modified PP separators (ci – ciii) during the course of lithium polysulfide diffusion from the left part to the right part of the U-shaped glass unit.

The superior polysulfide barrier effect through the STO-W/S hybrid engineered PP separator comparing with the STO-W modified PP separators and original PP separator can be directly confirmed by lithium polysulfide permeation measurements. As shown in **Figures 5ai, 5bi and 5ci**, initially, three specially designed U-shaped glass units coupled with the original PP, STO-W and STO-W/S hybrid modified PP in the middle, respectively, 0.025 mol $\cdot$ L^{-1} of Li_2S_6 tetrahydrofuran (THF) solution and pure THF were filled into the left and right tubes, respectively. With the extension of the dwell time, the Li_2S_6 obviously diffused from Li_2S_6 THF solution to pure THF in the cases of the PP separators, as seen in **Figures 5ai - 5aiii**. In contrast, only trace amounts of Li_2S_6 were passed through the STO-W modified PP separator

after 12 h (**Figures 5bi – 5biii**). As for the glass unit with STO-W/S hybrid modified PP separator, almost no Li_2S_6 diffusion from the left tube to right tube was observed from **Figures 5ci – 5ciii** even after 12 h. The superior performance of STO-W/S hybrid modified PP can be ascribed to the synergistic effect in terms of the strong chemical absorption capability and the permselective channels of the STO-W/S sandwiched nanostructure only for Li^+. This observation further implies that the PP separator simply engineered by the STO-W/S surface layer has a strong application potential for LSBs.

2.3. Electrochemical performance of PP separator modified with STO-W and STO-W/S

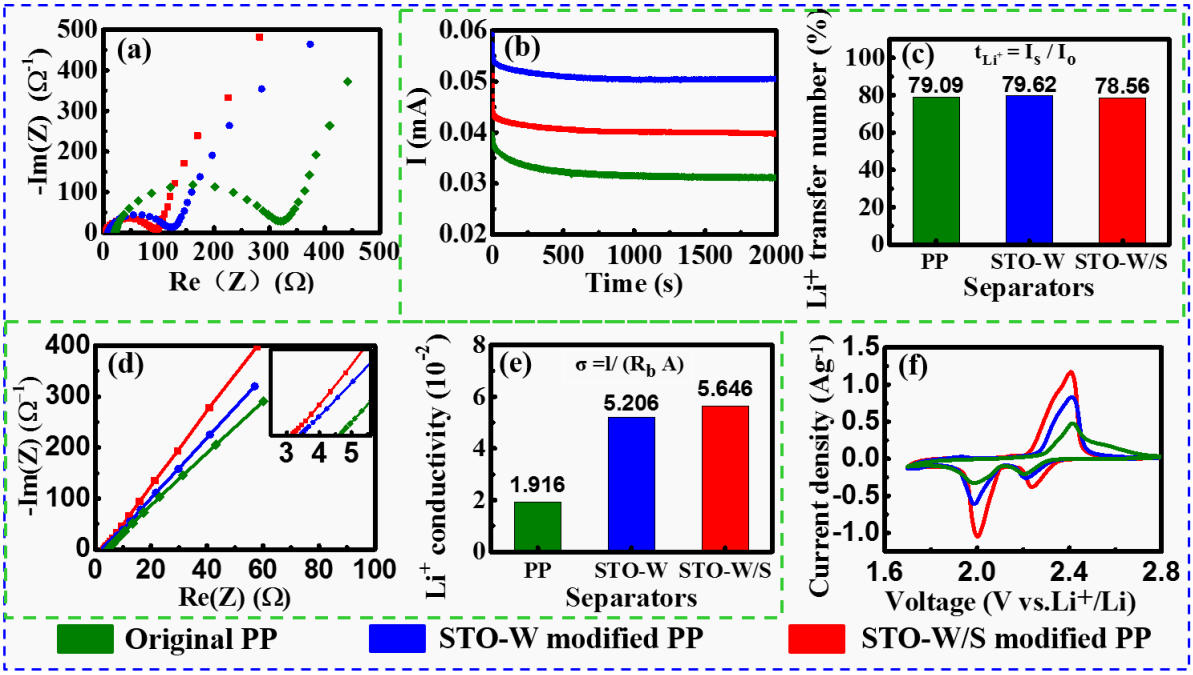

Figure 6. EIS (a) and CV (f) curves for LSBs coupled with PP separator, STO-W and STO-W/S modified PP separator; and: the obtained chronoamperometry profiles of two-electrode symmetrical lithium metal cells coupled with PP and modified PP separators (b) and the corresponding calculated Li^+ transference numbers(c); and: the obtained EIS profiles of two-electrode symmetrical stainless steel cells coupled with PP and modified PP separators (d) and the calculated corresponding Li^+ conductivity (e).

Electrochemical evaluations were conducted to validate the superiority of STO-W/S hybrids serving as lithium polysulfide permeation barrier layers for LSBs. Electrochemical impedance spectroscopy (EIS) results shown in **Figure 6a** indicate the LSBs coupled with the STO-W/S modified PP separator to exhibit smaller inner resistance. **Figures 6b** and **6c** show the observed chronoamperometry profiles and the calculated corresponding Li^+ transference numbers. The results indicate that the functional layers of STO-W and STO-W/S have no obvious influence on the Li^+ transference through the separator. Moreover, due to the much improved wettability to the electrolyte, STO-W/S and STO-W modified PP separator show higher Li^+ conductivity, as displayed in **Figures 6d** and **6e**. Cyclic voltammetry (CV) curves, given in **Figures 6f and S2**, confirm that LSBs coupled with STO-W/S and STO-W modified PP separator show higher electrochemical activity, reversibility and Li^+ diffusion coefficient (D_{Li^+}) than that of LSBs using commercially-available PP separators. The electrochemical measurement results summarized in **Table S1** further demonstrate that STO-W/S hybrid functional layer coated on PP not only have no adverse effect on the electrochemical performance, but also can effectively suppress the shuttle effect of LPSs and increase the electrochemical activity, reversibility and Li^+ conductivity.

To evaluate the applicability of the STO-W/S hybrid functional layer modified PP separator within LSBs, a series of LSBs using the controlled original PP, STO-W and STO-W/S modified PP film as separators were assembled in an Ar-filled glove box, respectively. Both the rate capability and cyclic performance were evaluated via galvanostatic charge/discharge measurement. As displayed in **Figure 7a**, the batteries with controlled original PP, STO-W and STO-W/S hybrid modified PP separators delivered an ascending rate capability, especially more conspicuous with the increase of the applied current density. The specific discharge capacities delivered by the batteries consisting of Li// PP with STO-W/S //S-C composite cathode are 1242, 1072, 830, 705, 603 and 492 $mAh \cdot g^{-1}$ at a current density of 0.1C, 0.2C, 0.5C, 1C, 1.5C and 2C rate, respectively. Typical charge and discharge voltage

profiles of Li// PP with STO-W/S //S-C batteries at different current densities (C-rates) and at various cycles, respectively, are as shown in **Figure. 7b**. **Figure 7c** present the charge/ discharge profiles of LSBs coupled with STO-W/S modified PP from 2nd to 100th cycles at 0.2 C. **Figure 7d** shows the cycling stability of LSBs coupled with PP, STO-W and STO-W/S modified PP at the same C-rate. This observation indicates that the application of STO-W/S modified PP as separator is helpful to achieve high capacity and good cyclic stability even at relatively low current density. As for LSBs coupled with STO-W/S modified PP separator at 1C rate, the initial capacity and the retained capacity after 500 cycles were ~ 813 and ~ 541 mAh g^{-1}, respectively (**Figure 7e**). The capacity fading rate was ~0.067% for each cycle.

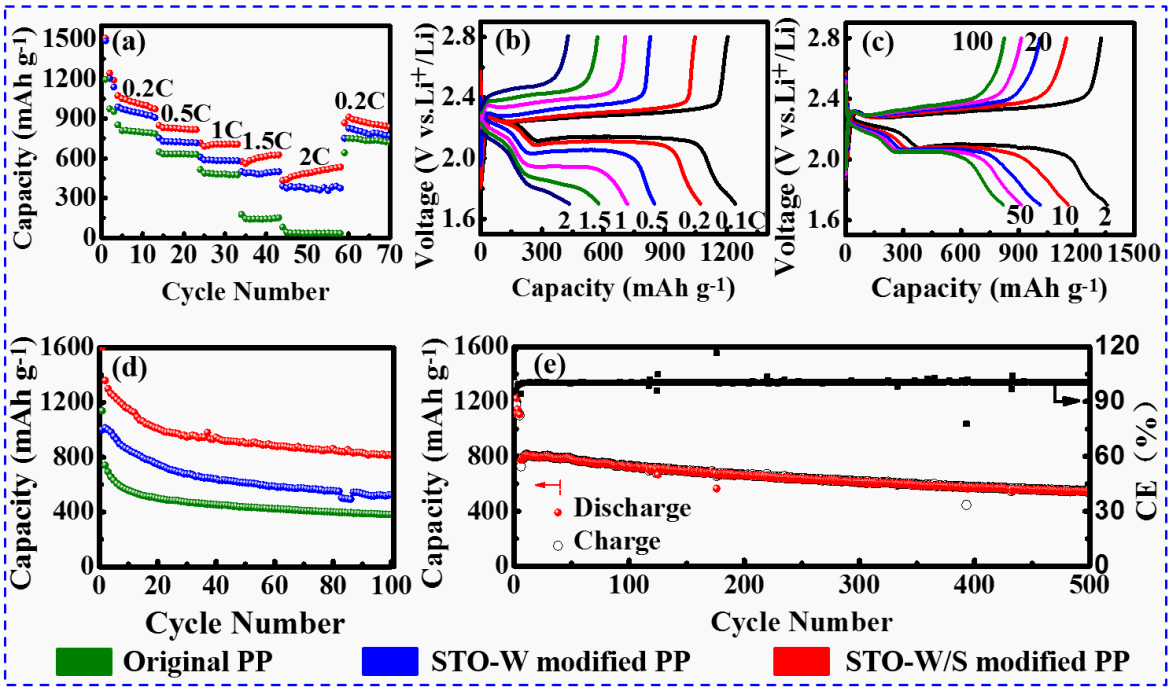

Figure 7. (a) The rate capabilities of LSBs coupled with PP, STO-W and STO-W/S modified PP separator, respectively; (b) Voltage charge/discharge profiles of LSBs coupled with STO-W/S modified PP from 0.1 to 2 C (here 1 C = 1675 mA·g^{-1}), respectively; (c) the charge/discharge profiles of LSBs coupled with STO-W/S modified PP from 2nd to 100th cycles at 0.2 C (d) Cyclic stabilities of LSBs coupled with PP, STO-W and STO-W/S modified PP at the *C*-rate of 0.2, respectively; (e) Long-term cyclic stability of LSBs coupled with STO-W/S modified PP at 1 C.

Table 1. Comprehensive comparison of the electrochemical performance of LSBs coupled with PP separators functionalized in different reported strategies and materials.

Functional layer on PP separators	Cathode & S loading (mg•cm^{-2})	Coating thickness [μm]	The 1st cycle capacity [mAh•g^{-1}]	Cycling property [mAh•g^{-1}]	Fading rate (%)	Refs.
STO-W/S hybrid	AC/S/AB/PVDF 0.8 ~ 1	4	812.7 [1 C]	541.4 [1C, 500 cycles]	0.067	this work
Black-phosphorus flakes	S/Super P/PVDF 1.5 ~ 2	0.4 mg•cm^{-1}	930 [0.4 Ag^{-1}]	800 [0.4 A•g^{-1}, 100 cycles]	0.139	[3]
MoS_2 layer	S/carbon/PVDF /	0.35	808 [0.5 C]	401 [0.5 C, 600 cycles)	0.083	[5]
Co/mSiO_2−NCNTs coating	S/Super P/PVDF 1.15	11.3	1005.2 [1 C]	774 [1C, 250 cycles]	0.09	[8]
Indium Nitride coating	S/Super P/PVDF 1.5	6.5	860.7 [1 C]	634.6 [1C, 1000 cycles]	0.026	[9]
$Li_4Ti_5O_{12}$ /graphene mixture	S/Super P/PVDF 1.0-1.2	35	813.3 [1 C]	697 [1C, 500 cycles]	0.028	[18]
TiO_2 decorated C coating	S/AB/gelatin 2.0	1.3	1227 [0.1 C]	883 [0.1C, 180 cycles]	0.156	[26]
SiO_2 nano-particles layer	CNTs/S/CB/PVDF 1.2-1.4	/	937 [0.2 C]	603.5 [0.2C, 200 cycles]	0.17	[30]

*AC: activated carbon; AB: acetylene black; CB: carbon black; CNTs: carbon nanotubes;

The achieved lithium-ion storage performance of LSBs coupled with STO-W/S modified PP separator are superior to LSBs coupled with original PP and PP separators modified by neat STO nanowires. The functional layer engineered on top of PP surface is thinner than most of most of the reported functional layers; however, as given in **Table 1**, the achieved fading rate for each cycle is comparable and even lower than most of the reported functional layers. As demonstrated in **Figure 1**, the observed superior capacity retention of LSBs coupled with STO-W/S modified PP separator at different C-rate can be attributed to the enhanced wettability to electrolyte, the improved Li^+ ion conductivity, the enhanced suppression of the shuttle of LPSs (thus regenerate the trapped LPSs with the synergistic effect of the sandwiched sheet/nanowire hybrid structure) and the strong chemical absorption capability of STO-W/S to LPSs.

4. Conclusion

In summary, sodium-containing titanium oxides nanowires (STO-W) and their hybrid with nanosheets (STO-W/S) have been developed through a scalable one-pot hydrothermal route. Using a flow-directed vacuum filtration method, uniform STO-W and STO-W/S functional layers with strong adhesion are also successfully assembled onto the surface of PP separators. It is worth mentioning that the electrolyte wettability and Li^+ conductivity of PP separators are significantly enhanced after being surface engineered by the polar STO-W and STO-W/S, respectively. Benefitting from the enhanced wettability to electrolyte, the improved Li^+ ion conductivity, the effective suppression to the 'shuttling' of LPSs (thus reutilization of the trapped LPSs with the synergistic effect of the sandwiched sheet/nanowire hybrid structure) and the strong chemical adsorption capability of STO-W/S to LPSs, lithium-sulfur batteries coupled with STO-W/S modified PP separator delivered an initial capacity of ~ 813 mAh g^{-1} at 1C rate with a capacity fading rate of ~0.067% per cycle. The capacity was still retained at ~ 541 mAh g^{-1}, even after 500 cycles. The observed lithium-ion storage performance and capacity retention of LSBs coupled with STO-W/S modified PP separator at various C-rates were superior to LSBs coupled with STO-W modified and original PP separator, as well as most of the previously reported functionalized PP separators. Therefore, the aforementioned advantages over commercial polypropylene (PP) separators, illustrate the newly-proposed functionalization strategy for separators as promising candidates for developing the next-generation multifunctional separators for high performance lithium-sulfur batteries.

Acknowledgements

This work was conducted under the auspices of the National Natural Science Foundation of China (61974072, 51772157), Natural Science Foundation of Jiangsu Province (BK20181396) and Major Basic Research Project of the Natural Science Foundation of the Jiangsu Higher Education Institutions (18KJB430020), Graduate Research & Innovation

Projects of Jiangsu Province (KYCX18_0847). Fund of NJUPT (NY217077, NY219110), Shuguang Program supported by Shanghai Education Development Foundation and Shanghai Municipal Education Commission (18SG035), Priority Academic Program Development of Jiangsu Higher Education Institutions (YX03003), Jiangsu National Synergistic Innovation Center for Advanced Materials. We acknowledge the proofreading and editing support provided Edfluent services for this paper.

References

[1] J.Q. Huang, Q. Zhang, F. Wei, *Energy Storage Mater*, 2015, **1**, 127-145.

[2] S.Y. Bai, X.Z. Liu, K. Zhu, S. Wu, H. Zhou, *Nat. Energy*, 2016, **1**, 16094.

[3] J. Sun, Y.M. Sun, M. Pasta, G.M. Zhou, Y.Z. Li, W. Liu, F. Xiong, Y. Cui, *Adv. Mater*, 2016, **28(44)**, 9797-9803.

[4] J. H. Kim, G. Y. Jung, Y. H. Lee, J. H. Kim, S. Y. Lee, S. K. Kwak, S. Y. Lee, *Nano Letter*, 2017, **17(4)**, 2220-2228.

[5] Z. A. Ghazi, X. He, A. M. Khattak, N. A. Khan, B. Liang, A. Iqbal, J.X. Wang, H. Sin, L.S. Li, Z.Y. Tang, *Adv. Mater*, 2017, **29(21)**, 1606817.

[6] M. S. Kim, L. Ma, S. Choudhury, L. A. Archer, *Adv. Mater. Interfaces*, 2016, **3(22)**, 1600450.

[7] H.J. Peng, Z.W. Zhang, J.Q. Huang, G. Zhang, J. Xie, W.T. Xu, J.L. Shi, X. Chen, X.B. Cheng, Q. Zhang, *Adv. Mater*, 2016, **28(43)**, 9551-9558.

[8] D.L. Fang, Y.L. Wang, X.Z. Liu, J. Yu, C. Qian, S.M. Chen, X. Wang, S.J. Zhang, *ACS Nano*, 2019, **13(2)**, 1563-1573.

[9] L.L. Zhang, X. Chen, F. Wan, Z.Q. Niu, Y.J. Wang, Q. Zhang, J. Chen, *ACS Nano*, 2018, **12(9)**, 9578-9586.

[10] T.Z Zhuang, J.Q. Huang, H.J. Peng, L.Y. He, X.B. Cheng, C.M. Chen, Q. Zhang, *Small*, 2016, **12(3)**, 381-389.

[11] Z.D. Huang, Y.W. Fang, M.T. Yang, J.K. Yang, Y.Z. Wang, Z. Wu, Q.C. Du, T. Masese, R.Q. Liu, X.S. Yang, C.H. Qian, S.W. Jin, Y.W. Ma, *ACS Appl. Mater. Interfaces*, 2019, **11(22)**, 20013-20021.

[12] Z.H. Sun, J.Q. Zhang, L.C. Yin, G.J. Hu, R.P. Fang, H.M. Cheng, F. Li, *Nat. Commun*, 2017, **8**, 14627.

[13] Z. W. Seh, W. Li, J. J. Cha, G.Y. Zheng, Y. Yang, M. T. McDowell, P. Chun Hsu, Y. Cui, *Nat. Commun*, 2013, **4**, 1331.

[14] T.H. Zhou, W. Lv, J. Li, G.M. Zhou, Y. Zhao, S.X. Fan, B.L. Liu, B.H. Li, F.Y. Kang and Q.H. Yang, *Energy Environ. Sci*, 2017, **10**, 1694-1703.

[15] J. Liang, Z.H. Sun, F. Li, H.M. Cheng, *Energy Storage Mater*, 2016, **2**, 76-106.

[16] T.J. Gao, T. H. Le, Y. Yang, Z.H. Yu, Z.H. Huang, F.Y. Kang, *Mater*, 2017, **10**, 376.

[17] H.B. Yao, K. Yan, W.Y. Li, G.Y. Zheng, D.S. Kong, Z. W. Seh, V. K. Narasimhan, Z. Liang, Y. Cui, *Energy Environ. Sci*, 2014, **7,** 3381-3390.

[18] Y. Zhao, M. Liu, W. Lv, Y. He, C. Wang, Q. Yun, B. Li, F. Kang, Q. Yang, *Nano Energy*, 2016, **30**, 1-8.

[19] T. Yim, S. H. Han, N. H. Park, M. Sik. Park, J. H. Lee, J. Shin, J. W. Choi, Y. Jung, Y. N. Jo, J. Yu, K. J. Kim, *Adv. Funct. Mater*, 2016, **26(43)**, 7817-7823.

[20] J.D. Zhu, Y.Q. Ge, D. Kim, Y. Lu, C. Chen, M.J. Jiang, X.W. Zhang, *Nano Energy*, 2016, **20**, 176-184.

[21] Z. Wang, M. Feng, H. Sun, G.R. Li, Q. Fu, H.B. Li, J. Liu, L.Q. Sun, A. Mauger, C. M. Julien, H.M. Xie, Z.W. Chen, *Nano Energy*, 2019, **59**, 390-398.

[22] Q.C. Du, M.T. Yang, J.K. Yang, P. Zhang, J.Q. Qi, L. Bai, Z. Li, J.Y. Chen, R.Q. Liu, X.M. Feng, Z.D. Huang, T. Masese, Y.W. Ma, W. Huang, *ACS Appl. Mater. Interfaces*, 2019, **11(38)**, 34895-34903.

[23] P. Joo H. Kim, J. Seo, K. Fu, J. h. Choi, Z.M. Liu, J. Kwon, L.B. Hu , U. Paik, *NPG Asia Mater*, 2017, **9**, e375.

[24] Z.X. Hao, L.X. Yuan, Z. Li, J. Liu, J.W. Xiang, C. Wu, R. Zeng, Y.H. Huang, *Electrochim. Acta*, 2016, **200**, 197-203.

[25] F.Q. Li, G.C. Wang, P. Wang, J. Yang, K. Zhang, Y.X. Liu, Y.Q. Lai, *J. Electroanal. Chem*, 2017, **788**, 150-155.

[26] H.Y. Shao, W.K. Wang, H. Zhang, A.B. Wang, X.N. Chen, Y.Q. Huang, *J. Power Sources*, 2018, **378**, 537-545.

[27] J.J. Song, D.W. Su, J.J. Song, D.W. Su, X.Q. Xie, X. Guo, W.Z. Bao, G.J. Shao, G.X. Wang, *ACS Appl. Mater. Interfaces*, 2016, **8**, 29427-29433.

[28] G.Q. Ma, F.F. Huang, Z.Y. Wen, Q.S. Wang, X.H. Hong, J. Jin, X.W. Wu, *J. Mater. Chem. A*, 2016, **4**, 16968-16974.

[29] H.W. Wu, Y. Huang, W.C. Zhang, X. Sun, Y.W. Yang, L. Wang, M. Zong, *J. Alloys and Compd*, 2017, **708**, 743-750.

[30] J. Li, Y.D. Huang, S. Zhang, W. Jia, X.C. Wang, Y. Guo, D.Z. Jia, L.S. Wang, *ACS Appl. Mater. Interfaces*, 2017, **9(8)**, 7499-7504.

[31] Y.Z. Wang, W.H. Liu, R.Q. Liu, P.F. Pan, L.Y. Suo, J.Y. Chen, X.M. Feng, X.Z. Wang, Y.W. Ma, W. Huang., *New J. Chem*, 2019, **43,** 14708-14713.

[32] Z.D. Huang, B. Zhang, S.W. Oh, Q.B. Zheng, X.Y. Lin, N. Yousefi, J. Kyo. Kim, *J. Mater. Chem*, 2012, **22**, 3591-3599.

[33] K. Prasanna, C. S. Kim, C. W. Lee, *Mater. Chem. Phys*, 2014, **146**, 545-550.

[34] J.D. Zhu, C. Chen, Y. Lu, J. Zang, M.J. Jiang, D. Kim, X.W. Zhang, *Carbon*, 2016, **101**, 272-280.

[35] J.Q. Huang, T.Z. Zhuang, Q. Zhang, H.J. Peng, C.M. Chen, F. Wei, *ACS Nano*, 2015, **9(3)**, 3002-3011.

Supplementary information

Mitigating the Polysulfides "Shuttling" with TiO_2 Nanowires/Nanosheets Hybrid Modified Separators for Robust Lithium-Sulfur Batteries

Zhen-Dong Huang,‡ Ming-Tong Yang,‡ Ju-Quan Qi, Pei Zhang, Linna Lei, Qing-Chuan Du, Ling Bai, Hui Fu, Xu-Sheng Yang, Rui-Qing Liu, Titus Masese, Haijiao Zhang,* and Yan-Wen Ma**

Dr. Z. D. Huang 1, M. T. Yang 2, J. Q. Qi 3, P. Zhang 4, L. N. Lei 5, Q. C. Du 6, L. Bai 7, Dr. R. Q. Liu 10, Prof. Y. W. Ma 13
Key Laboratory for Organic Electronics and Information Displays & Jiangsu Key Laboratory for Biosensors, Institute of Advanced Materials (IAM), Jiangsu National Synergetic Innovation Center for Advanced Materials (SICAM), Nanjing University of Posts and Telecommunications, 9 Wenyuan Road, Nanjing 210023, P.R. China
E-mail: iamywma@njupt.edu.cn
Dr. H. F. Fu 8, Dr. X. S. Yang 9,
Department of Industrial and Systems Engineering, Hong Kong Polytechnic University, Hung Hom, Kowloon, Hong Kong, P.R. China
Hong Kong Polytechnic University Shenzhen Research Institute, Shenzhen, 518057, P.R. China
Dr. T. Masese 11
Research Institute of Electrochemical Energy, National Institute of Advanced Industrial Science and Technology (AIST), Ikeda, Osaka 563-8577, Japan
E-mail: titus.masese@aist.go.jp
Prof. H. J. Zhang 12
Institute of Nanochemistry and Nanobiology, Shanghai University, Shanghai 200444, P. R. China
E-mail: hjzhang128@shu.edu.cn

1. Additional experimental details

Visual permeation tests of 0.025 mol·L^{-1} Li_2S_6 solution in tetrahydrofuran were conducted in a U-shaped glass unit isolated by a piece of PP, STO-W and STO-S/W modified PP separators to analyse the barrier performance of the STO-W and STO-S/W modified PP separators over PP separator.

To test the **wettability** of PP, STO-W and STO-S/W modified PP separators against the electrolyte of 1 mol·L^{-1} LiTFSI dissolved in 1, 2-dimethoxyethane/1, 3- dioxolane (DOL : DME = 1 : 1 by volume) with 1 % $LiNO_3$ additive, the contact angles of the applied electrolyte to the corresponding separators were analyzed by using a drop shape analysis system (KRUSS DSA20).

In order to analyze **the ionic conductivities** of the PP, STO-W and STO-S/W modified PP separators, electrochemical impedance spectroscopy (EIS) was measured in coin type two-electrode cell (CR2032) systems with two stainless steel discs as the working electrode and counter electrode, respectively. The PP, STO-W and STO-S/W modified PP infused with the electrolyte of 1 mol·L^{-1} LiTFSI dissolved in 1, 2-dimethoxyethane/1, 3- dioxolane (DOL : DME = 1 : 1 by volume) with 1 % $LiNO_3$ additive were used as separator in between the stainless steel electrodes. Electrochemical impedance spectroscopy (EIS) measurements was carried out using a multi-channel electrochemical workstation (Bio-Logic EC-Lab, VMP3) within the frequency ranging from 1 MHz to 1 Hz under the potential amplitude of 10 mV. Finally, the lithium ionic conductivity through above separators was calculated by following the equation (1) below: [1]

$$\sigma = l/RS \quad (1)$$

where *l* is the thickness of the separator, *S* is the contact area and *R* is the bulk resistance.

To determine the **lithium-ion transference number** for PP, STO-W and STO-S/W modified PP separators, chronoamperometry measurements were conducted in coin type two-electrode cell (CR2032) systems with two lithium metal electrodes as the working electrode and counter electrode, respectively, using an electrochemical working station at a constant step potential of 10 mV. The PP, STO-W and STO-S/W modified PP infused with the electrolyte of 1 $mol \cdot L^{-1}$ LiTFSI dissolved in 1, 2-dimethoxyethane/1, 3- dioxolane (DOL : DME = 1 : 1 by volume) with 1 % $LiNO_3$ additive were used as separator sandwiched between the lithium metal electrodes. The corresponding lithium-ion transference numbers were calculated from the ratio of steady state current to initial state current based on the equation 2: [2]

$$t_{Li+} = I_s / I_o \quad (2)$$

where t_{Li+} is the transference number, while I_s and I_o represent the current at the steady state and initial state, respectively.

Lithium-ion diffusion coefficients for PP, STO-W and STO-S/W modified PP separators were calculated by a series of cyclic voltammograms at a scanning rate varied from 0.03 ~ 0.4 mV s^{-1} in a voltage window of 1.7–2.8 V. By following the Randles-Sevick equation as given below: [3]

$$I_p = 2.69 \times 10^5 \cdot n^{1.5} \cdot A D_{Li+}^{0.5} C_{Li} v^{0.5} \quad (3)$$

in which D_{Li+} stands for lithium-ion diffusion coefficient ($cm^2 \bullet s^{-1}$), I_p is the value of the corresponding peak current in ampere (*A*), *n* is the number of electrons caused by

the reaction (n = 2 for LSBs), A, C_{Li} and v are the area of electrode (cm^2), the concentration of Li^+ ($mol \cdot L^{-1}$) and the scanning rate ($V \cdot s^{-1}$), respectively.

2. Additional experimental results

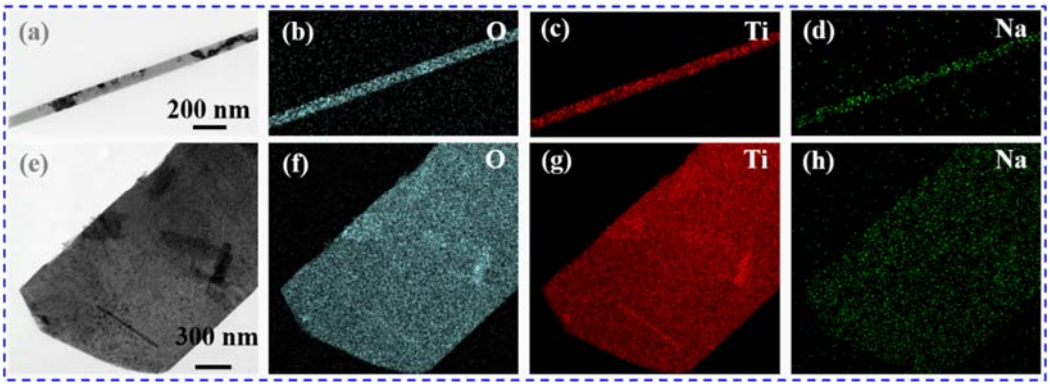

Figure S1. S/TEM images and the corresponding element mapping images of O, Ti and Na within STO-W (a, b, c, d) and STO-S (e, f, g, h), respectively.

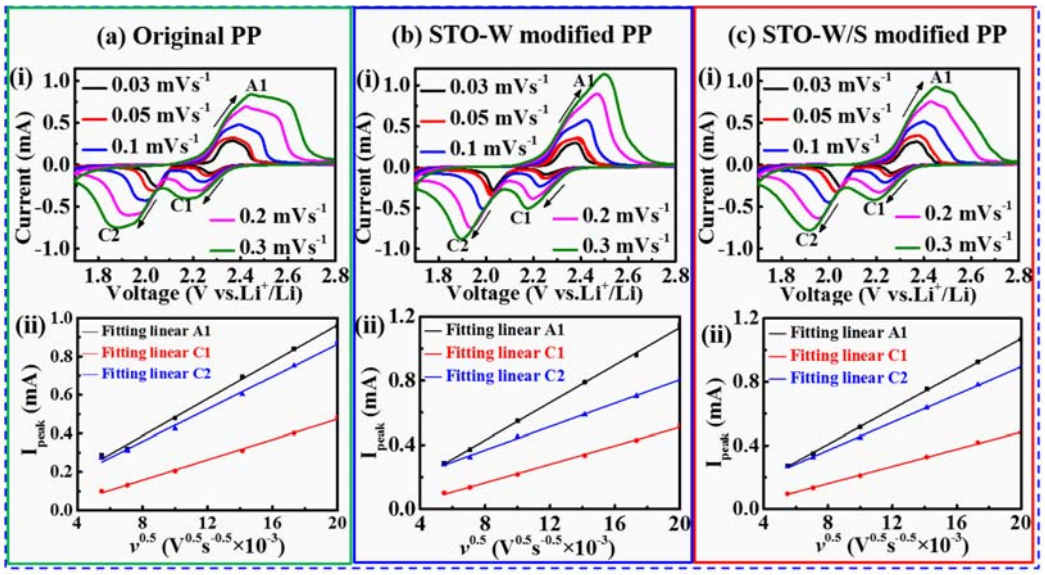

Figure S2. The cyclic voltammetry curves at different scanning rate (i) and the linear relation profiles of peak current vs square root of scanning rate (ii) corresponding to the lithium sulfur batteries with original PP separator (a), PP separator modified with STO-W (b) and STO-W/S (c), respectively.

Table S1. A summary of the physicochemistry properties of original PP separator (a), PP separator modified with STO-W (b) and STO-W/S (c) within lithium sulfur batteries.

Calculated parameters	PP	STO-W modified PP	STO-W/S modified PP
Li^+ conductivity (mS cm^{-1})	1.92×10^{-2}	5.21×10^{-2}	5.65×10^{-2}
Li^+ transfer number	0.7909	0.7962	0.7856
Resistance (ohm)	320.057	125.366	94.148
D_{Li+} at Peak A1 (cm^2 s^{-1})	3.12×10^{-9}	4.63×10^{-9}	4.15×10^{-9}
D_{Li+} at Peak C1 (cm^2 s^{-1})	0.94×10^{-9}	1.11×10^{-9}	0.98×10^{-9}
D_{Li+} at Peak C2 (cm^2 s^{-1})	2.39×10^{-9}	1.80×10^{-9}	2.58×10^{-9}

References

[1] K. Prasanna, C. S. Kim, C. W. Lee, *Mater. Chem. Phys*, 2014, **146**, 545-550.

[2] J.D. Zhu, C. Chen, Y. Lu, J. Zang, M.J. Jiang, D. Kim, X.W. Zhang, *Carbon*, 2016, **101**, 272-280.

[3] J.Q. Huang, T.Z. Zhuang, Q. Zhang, H.J. Peng, C.M. Chen, F. Wei, *ACS Nano*, 2015, **9(3)**, 3002-3011.